Macromolecules

Open Access

pubs.acs.org/Macromolecules

Article

Poly-3-hydroxybutyrate, a Crystal-Mobile Biodegradable Polyester

Afiq Anuar, Qiang Yu, Katalee Jariyavidyanont, Albrecht Petzold, René Androsch, Thomas Thurn-Albrecht,* and Kay Saalwächter*

Cite This: *Macromolecules* 2024, 57, 8507−8518

Read Online

ACCESS | Metrics & More | Article Recommendations | Supporting Information

ABSTRACT: Poly(3-hydroxybutyrate) (P3HB), a biodegradable thermoplastic with the potential to partially replace oil-based commodities, suffers from embrittlement over storage time. We here investigate possible causes by monitoring aging processes in the sample through changes in mechanical and thermal properties as well as the semicrystalline morphology (crystallinity, lamellar stack dimensions, and its inhomogeneity) over time, using advanced small-angle X-ray scattering analyses for the latter. We find that the slow rise in the shear modulus of the materials is accompanied by secondary crystallization, detected as lamellar thickening and an increase in the melting point. These morphology changes may be due to the chain mobility in the crystallites. This is a feature of "crystal-mobile" polymers that are known to be able to crystallize more fully than their crystal-fixed counterparts. We present the first evidence of the related crystalline α_c relaxation in P3HB by dynamic-mechanical analysis (DMA) and investigate the process microscopically by advanced magic-angle spinning solid-state exchange NMR techniques, specifically centerband-only detection of exchange. We show that monomer jumps in the P3HB crystals are comparably slow (i.e., with an average correlation time τ_c of 0.1 s at 120 °C). Their apparent activation energy (80 to 90 kJ/mol) is found to be independent of the crystallization temperature and in good agreement with the DMA results.

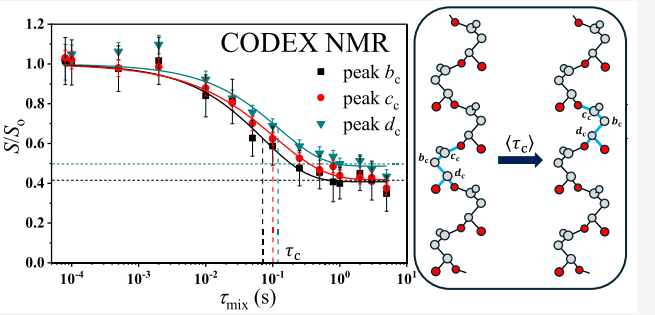

INTRODUCTION

Poly(3-hydroxybutyrate) (P3HB) is one of the most commonly biosynthesized polyhydroxyalkoates (PHA), produced through bacterial fermentation.[1,2] Due to its accessibility for mass production, environmental friendliness, high elastic modulus, and high melting point, P3HB has received much attention as a potential candidate for sustainable biodegradable polymers to replace petroleum-based polymers.[1−3] P3HB has been reported for use in medical packaging, tissue engineering, and drug delivery due to its biocompatibility and nontoxicity, but its wider commercialization is challenged by detrimental embrittlement over time.[3−5]

Many researchers have conducted studies into the factors that drive P3HB embrittlement.[3,6−8] The prevailing opinions lean toward either the physical aging of amorphous parts below their glass transition temperature (T_g) or secondary crystallization. Based on these insights, several approaches, including blending with other polymers, plasticizers, and lubricants, have been proposed to avoid physical aging by lowering T_g.[9−13] More popular approaches involve copolymerization, which has been reported to improve ductility by modifying its semicrystalline structure and avoiding secondary crystallization.[14−25] While these approaches can improve mechanical properties at least transiently, they may not always be the most effective and economical choices.[9−25] Certain polyesters like poly(ethylene terephthalate) or stereoregular poly(lactic acid), PLA, are inherently brittle due to their high T_g,[26] and can benefit from novel processing strategies such as cold crystallization of the melt, stretching, and quenching. P3HB has a significantly lower T_g, possibly enabling alternative treatments. However, such improvements are possible only with a comprehensive microscopic understanding of semicrystalline structure formation and evolution, in particular during sample aging.

For P3HB, detailed insights regarding its detailed semicrystalline morphology (in terms of dimensions and inhomogeneity of the lamellar stack) and potential intracrystalline chain dynamics (ICD) are still missing.[3,14] As we know, the mechanical properties of semicrystalline polymers are influenced by the extent of ICD.[27] They can be classified as either crystal-fixed or crystal-mobile, based on the absence or presence of ICD, respectively.[27] A recent study by Xia et al.[14] suggested that P3HB may belong to the class of crystal-fixed polymers due to undetectable ICDs within 500 ms up to 100 °C in their P3HB and P(3HB-co-4HD) samples. We will show

Received: April 24, 2024
Revised: August 6, 2024
Accepted: August 6, 2024
Published: August 20, 2024

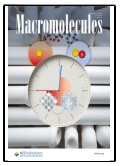

here that P3HB does feature a rather slow ICD, which could contribute to the embrittlement of P3HB even at ambient temperature.

In this work, we monitor long-time changes in the semicrystalline structure by low-resolution ^{1}H NMR providing a mobility-based measure of crystallinity and small-angle X-ray scattering (SAXS) with advanced data treatment providing not only the domain thicknesses but also information about their inhomogeneous distribution. The mode of secondary crystallization, either lamellar thickening or crystal insertion,[28] is further characterized by fast scanning calorimetry (FSC) measurements. Dynamic-mechanical analysis (DMA) is used to assess long-time changes in the shear modulus of the material as well as to identify the crystalline α_c process attributed to chain diffusion through the crystals and determine its apparent activation energy by time−temperature superposition (TTS) of the frequency-dependent mechanical response.

^{13}C magic-angle spinning (MAS) nuclear magnetic resonance (NMR) is used to probe directly the diffusive exchange between the crystalline and the amorphous regions by monitoring the T_1 relaxation decay, while the monomer jump time is probed by a MAS-based ^{13}C exchange NMR technique, specifically centerband-only detection of exchange (CODEX).[29] Overall, we identify a lamellar thickening process as the specific mechanism of secondary crystallization that parallels the long-time increase in the shear modulus of P3HB. Intracrystalline dynamics is identified as its molecular origin and characterized in detail with regard to its time scale and apparent activation energy. We discuss possible relations to the enhanced brittle fracture, and we hope that our insights can provide valuable guidance for refining processing techniques and exploring copolymerization strategies, thereby advancing the use of P3HB-based polymers as sustainable alternatives to current fossil-based polymers.

EXPERIMENTAL SECTION

Materials. P3HB without a nucleating agent (P338 as pellets, lot 26T3380) was obtained from Biomer (Schwalbach, Germany). The same base polymer (P338) was reported to have an M_n of 130 kDa.[30] For other P3HB products from Biomer (P209 and P309) with similar M_n, the polydispersity (M_w/M_n) was determined to be around 4.[31] P3HB is subjected to thermal degradation at and above its melting temperature.[32] In our hands, differential scanning calorimetry (DSC) experiments shown in the Supporting Information (SI), Figure S1, revealed changes in the melting point upon repeated heating and cooling cycles, which may be taken as an indirect hint at sample degradation. To exclude such effects from our analyses, each measurement was performed with a new sample.

Dynamic Mechanical Analysis. DMA experiments to determine the shear modulus were conducted with an Ares G2 rheometer (TA Instruments, Eschborn, Germany) equipped with a climate chamber in a strip geometry (sample length between clamps 20 mm, width 10 mm, thickness 1.0 mm) at a strain amplitude of 0.1%. Real-time aging experiments were conducted at 10 rad/s at 60 °C, and frequency sweeps were conducted from 0.1 to 100 rad/s in a temperature range between 60 and 150 °C. Samples were prepared by both isothermal crystallization at 120 °C for 1 h (for aging experiments) and nonisothermal crystallization upon cooling with −5 K/min (for frequency sweeps) in rectangular molds and always installed in the rheometer at room temperature.

Tensile Testing. Stress−strain measurements were performed with a Linkam tensile-stage TST350 instrument (Tadworth, UK) equipped with a 200 N load cell. Due to the low nucleation rate at 120 °C,[33] a direct melt crystallization leads to millimeter-sized spherulites, which does not allow for further tensile testing. For this reason, P3HB films were prepared by cold crystallization, where a low-temperature crystal nucleation step at 25 °C for 1 min is included before isothermally crystallizing the sample at 120 °C for 7 min. P3HB films with a thickness of about 200 μm were punched into a dumbbell-shaped specimen with a gauge length of 5 mm and a gauge width of 2 mm. The experiment was performed at room temperature (26 ± 2 °C) at a constant cross-head speed of 5 μm/s and with a preload of 0.2 N. All measurements were carried out within 5 min after sample preparation or thermal treatment to avoid physical aging or annealing effects.[34] The results for the ultimate properties were averaged over at least 5 samples.

Small-angle X-ray Scattering. SAXS measurements to probe the structure of the lamellar stacks were performed on a Kratky compact camera (Anton Paar GmbH, Graz, Austria) equipped with X-ray optics (AXO Dresden GmbH, Germany) and a temperature-controlled sample holder and 1D detector Mythen2 R 1K (Dectris, Switzerland). The sample was quenched from the melt state (190 °C) to 120 °C within the Kratky camera, corresponding to an estimated cooling rate of 5 K/min. The exposure time for each measurement was 10 min. The analysis of the SAXS data is based on the interface distribution function (IDF or $K''(z)$), originally introduced by Ruland.[35] The detailed analysis procedure is described in our previous publications.[36−38] We here give a brief account of the method. The IDF or $K''(z)$ is well-suited for the description of the semicrystalline morphology of the polymer because of the presence of alternating stacks of amorphous and crystalline regions and the sharp interfaces between the two regions:

$$K''(z) = \frac{O_s \Delta\rho^2}{2}(h_a(z) + h_c(z) - 2h_{ac}(z) + h_{aca}(z) + \cdots) \quad (1)$$

with

$$h_{a,c}(z) = \frac{1}{\sqrt{2\pi}\,\sigma_{a,c}} e^{-(z-d_{a,c})^2/2\sigma_{a,c}^2} \quad (2)$$

where $d_{a,c}$ are the mean values and $\sigma_{a,c}$ are the widths of the thickness distributions. The higher-order distributions $h_{aca}(z)$ etc. are convolutions of the fundamental ones. After background subtraction, $K''(z)$ is related to the SAXS experimental data according to

$$K''(z) = 16\pi^3 \int_0^\infty [\lim_{s\to\infty} I(s)s^4 - I(s)s^4]\cos(2\pi sz)\mathrm{d}s \quad (3)$$

where $s = \frac{2}{\lambda}\sin\theta$ is the scattering vector, $\lim_{s\to\infty} I(s)s^4$ is the Porod parameter P (reflecting the total specific interfacial area in the sample), with the condition of $K''(0) = 0$. To suppress the noise at high scattering vectors, eq 3 is multiplied by a window function $G(s) = e^{-4\pi^2 s^2 \sigma^2}$, where σ is its width (σ = 0.4 nm was always used in this study). After the cosine transform, $K''(z)$ (eq 1) is fitted to the integrand of eq 3 taking the window function into account, so as to determine the fitting parameters d_c, d_a, σ_c, and σ_a. A detailed analysis example of one sample is shown in Figure S2 of the Supporting Information.

Differential Scanning Calorimetry. A Flash DSC 2 (Mettler-Toledo, Greifensee, Switzerland) was operated with the UFS 1 chip sensor and in combination with a TC 100 intracooler (Huber, Offenbach, Germany) for the investigation of secondary crystallization by observation of the melting temperatures of the formed crystals. The sample support temperature was kept constant at −90 °C and the sensor compartment was purged with nitrogen at a flow rate of 40 mL/min. Thin sections with a thickness of about 10 μm were cut from as-received pellets using a rotary microtome (Slee, Mainz, Germany) and then trimmed to a lateral size of 50−100 μm using a stereomicroscope and a scalpel. Before the sample was placed onto the chip sensor, a thin layer of silicone oil was spread on the sensor, followed by placing a layer of gold foil. Such a step assures optimum thermal contact between the sample and the sensor and also reduces mechanical distortion of the sensor membrane during the heating and cooling of the sample.

https://doi.org/10.1021/acs.macromol.4c00938
Macromolecules 2024, 57, 8507−8518

^{1}H Low-resolution NMR FID Analysis. ^{1}H time-domain NMR experiments to provide a mobility-based measure of absolute weight-based crystallinity by "proton counting" were conducted on a Bruker Minispec mq20 spectrometer with a proton frequency of about 20 MHz ($B_0 \approx 0.47$ T) by using a static probe head. Temperature regulation via a regulated airflow is provided by a BVT3000 unit with an accuracy of about ±1 K and a gradient of up to 0.5 K across the sample. Prior to isothermal crystallization, the samples were molten at 180 °C for ∼5 min as a compromise between the removal of thermal history and thermal degradation. Stepwise cooling and heating runs were performed starting from the sample's isothermal crystallization temperature at a rate of ∼5 K/min, with an additional 10 min of equilibration before each free-induction decay (FID) measurement.

The 90 and 180° pulse lengths ranged from 1.5 to 1.8 μs and from 3.5 to 3.7 μs, respectively. The time between successive scans (recycle delay) was set between 1.5 and 4 s, which is about 5 times the longer ^{1}H T_1 relaxation time of the crystalline domain to ensure full ^{1}H magnetization at any given temperature. As the instrument features a dead time of 15 μs, the FID signal detected directly after 90° lacks valuable information on the quickly decaying crystalline signal, requiring another experiment termed magic-sandwich echo (MSE).[39] Although the latter compensates for the dead time, its signal amplitude is reduced by pulse sequence imperfections and potential intermediate motions in the sample.[40−42] Thus, only the shape parameters were extracted from the MSE-FIDs while the signal amplitudes were taken from the fits to the FIDs. Sample data are shown in Figure 1.

The crystallinity determination is based upon the strong ^{1}H−^{1}H dipole−dipole couplings in the rigid crystals, leading to the fast decay of the respective signal. Averaging of these orientation-dependent interactions by fast segmental dynamics in the amorphous phase leads to the appearance of a distinguishable second component with a longer decay time (long T_2 relaxation time). The amplitudes of overall three distinguishable components of the FID, including an interphase often attributed to a rigid-amorphous fraction, are obtained by fitting the signal to the following empirical function,[40]

$$I_{\mathrm{FID}}(t) = A_{\mathrm{c}} \cdot e^{-(a^2 t^2/2)} \cdot \frac{\sin(b \cdot t)}{b \cdot t} + A_{\mathrm{i}} \cdot e^{-(t/T_{2,\mathrm{i}}^{*})^{\upsilon_{\mathrm{i}}}} + A_{\mathrm{a}} \cdot e^{-(t/T_{2,\mathrm{a}}^{*})^{\upsilon_{\mathrm{a}}}} \tag{4}$$

where t is the acquisition time, $A_{\mathrm{c,i,a}}$ is the amplitude of the corresponding relaxation component (being proportional to proton number), and $T_{2,\mathrm{i,a}}^{*}$ and $\upsilon_{\mathrm{a,i}}$ are the shape parameters (apparent T_2 and stretching exponents υ, respectively) of the more mobile components. The shape parameters a and b characterize the crystalline part, where the so-called Abragamian function works well for polymers with only CH_2 groups along the main chain. Figure 1 shows an example of the MSE-FID and FID curve fitting. The crystalline fraction is calculated according to

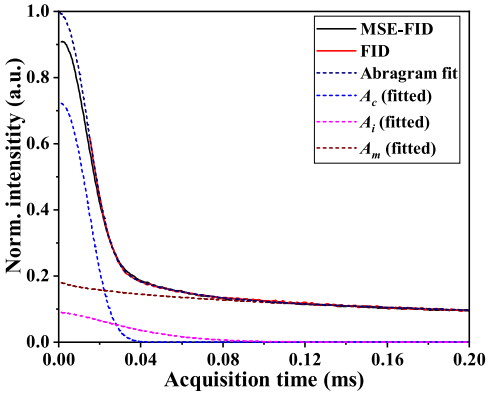

Figure 1. (a) Decomposition of the ^{1}H FID of P3HB crystallized and measured at 140 °C.

$$f_{\mathrm{c}} = \frac{A_{\mathrm{c}}}{A_{\mathrm{c}} + A_{\mathrm{i}} + A_{\mathrm{a}}} \tag{5}$$

^{13}C MAS NMR. All ^{13}C NMR measurements, allowing for chemical-shift resolved studies of molecular dynamics were conducted on a 400 MHz Bruker Avance III spectrometer with a ^{13}C Larmor frequency of 100.6 MHz using 4 mm double- and triple-resonance magic angle spinning (MAS) probes at a spinning frequency of 10,000 ± 3 Hz. The transmitter power used for ^{1}H and ^{13}C was around 40 and 140 W, respectively, corresponding to pulse lengths of around 3 μs on both channels. ^{13}C cross-polarization (CP) spectra rely on the ^{1}H−^{13}C dipolar polarization transfer, which is less efficient for more mobile chains. In a part of this work, we used very short contact times of 0.01 ms to polarize almost exclusively the crystalline component. ^{13}C direct polarization (DP) spectra with a short recycle delay of about 1 s in turn emphasize the mobile moieties in a sample featuring a comparatively short T_1 relaxation time.

Slow Molecular Rotations. Rotor-synchronized ^{13}C centerband-only detection of exchange (CODEX) experiments[29] reveal slow motions of the different chemical groups relying on the rotation of the chemical-shift anisotropy (CSA) tensors. It has often been used to investigate slow dynamics in semicrystalline polymers.[29] The CSA information is normally lost under MAS conditions but can be selectively reintroduced (recoupled) using rotor-synchronized π pulses spaced by half a rotor period τ_{r} in a dephasing and an equally long rephasing period before and after a mixing time τ_{mix}. If no reorientation of the CSA tensor occurs during τ_{mix}, then the signal will be completely refocused, while molecular rotations during τ_{mix} lead to a signal decay of the exchange intensity, $S(\tau_{\mathrm{mix}})$. A reference signal, S_0 is acquired with a short τ_{mix} (but using the same long τ_{mix} as the waiting time in a final z-filter) to compensate for signal losses caused by T_1 relaxation. To analyze the relevant correlation time τ_{c} describing the intracrystalline dynamics, the signal decay $S(\tau_{\mathrm{mix}})/S_0$ was fitted to a stretched exponential function decaying to a plateau, see ref 29,

$$S(\tau_{\mathrm{mix}})/S_0 = p + (1 - p) \cdot \exp[-(\tau_{\mathrm{mix}}/\tau_{\mathrm{c}}^{\mathrm{KWW}})^{\beta}] \tag{6}$$

where $p = 1/M$ with M distinguishable sites ($M = 2$ for the 2_1-helix in P3HB). CODEX was performed using the triple-resonance probe at 10 kHz MAS; high-power proton decoupling (SPINAL64)[43] was employed during the evolution and acquisition of the ^{13}C signal. The $\pi/2$ pulses for ^{1}H and ^{13}C were set to 3.0 and 3.4−3.6 μs, respectively. The required recoupled evolution time, $N\tau_{\mathrm{r}}$ depends on the magnitude of the CSA tensor and the reorientation angle. After an experimental assessment discussed below, it was set to 0.3 ms with τ_{r} = 100 μs and N being an integer. The recycle delay and contact times were 4−8 s and 1.7 ms, respectively.

T_1 Relaxation and Diffusive Exchange. ^{13}C T_1 relaxation is probed via decay during a z-filter of duration τ on the ^{13}C channel by Torchia's pulse sequence,[44] in which a short CP (10 μs) is utilized to emphasize the crystalline signal. The experiment has the advantage of providing signal decay function $I(\tau)$ with a well-defined limiting value of zero intensity. The decay not only reflects actual exponential T_1 relaxation, which is rather (often immeasurably) long but also a diffusive decay due to chain motion into the amorphous phase, where T_1 relaxation is almost instantaneous by comparison.[45] A linear decay on a $\sqrt{\tau}$ scale is immediately indicative of such diffusive behavior. As explained below, a power-law exponent of $\frac{1}{2}$ can be easily distinguished from an exponential process with linear τ dependence in the short-time limit in a double-logarithmic plot of $1 - I(\tau)/I(\tau = 0)$ vs τ.

RESULTS AND DISCUSSION

Mechanical Properties. In order to confirm the embrittlement of the P3HB sample over time, several mechanical measurements were conducted at room temperature. Stress−strain curves were utilized to observe storage effects on isothermally crystallized P3HB samples, as illustrated in Figure 2 and summarized in Table 1. In these measure-

https://doi.org/10.1021/acs.macromol.4c00938
Macromolecules 2024, 57, 8507−8518

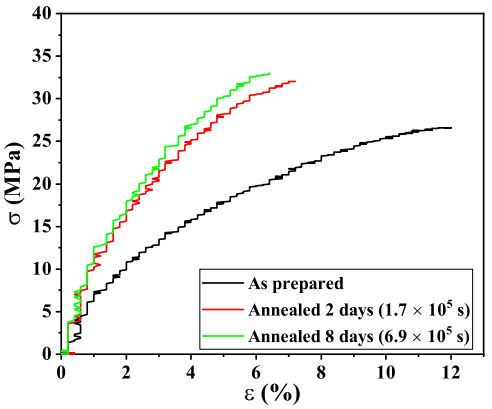

Figure 2. Exemplary stress−strain curves of P3HB, crystallized isothermally at 120 °C without and with annealing at 60 °C, all measured after cooling to room temperature within 5 min.

Table 1. Strain at Break (ϵ_B) and Stress at Break (σ_B) after Different Thermal Treatments

sample treatment	ϵ_B (%)	σ_B (MPa)
as-prepared	12.22 ± 0.62	26.06
annealed 2 days at 60 °C	7.18 ± 0.15	32.05
annealed 8 days at 60 °C	6.46 ± 0.38	33.00

ments, the "as-prepared" sample was crystallized at 120 °C and then subjected to stress−strain measurements without aging. The crystallization temperature was chosen based on the DSC measurements (see Figure S1). The strain at break (ϵ_B) of the as-prepared sample was 12.22%. Two days of annealing at 60 °C leads to a reduction of ϵ_B to 7.18%, which is further reduced to 6.46% after 8 days. The T_g of the amorphous phase of P3HB is reported in a range of about 0 to 27 °C,[34,46,47] where the variation may be attributed to confinement effects in the small amorphous domains. Since our annealing temperature is well above this range, we take this as an indication that actual aging effects in still glassy amorphous domains are at least an unlikely cause of embrittlement over time. Of course, the sluggish dynamics in the amorphous phase being close to T_g at ambient temperature, and even a slight increase related to the thickening of the crystalline lamellae could well affect the overall brittleness.

Further DMA measurements were conducted during 2 days of annealing at 60 °C after isothermal crystallization at 120 °C, comparable to the conditions in Figure 2. Figure 3a shows a slow increase and decrease of G' and G'' over time, respectively. The increase of G' reflects a stiffness increase that is consistent with the increase of the slope of the stress−strain curve, as shown in Figure 2.

Another important mechanical feature of P3HB can be seen from the DMA frequency and temperature sweeps. From such a data set, measured on a compression-molded specimen of nonisothermally crystallized P3HB, Figure 3b illustrates the temperature effect at a fixed frequency of 0.1 rad/s. The loss modulus G'' and tan δ showed a broad peak starting from around 40 °C that is typically observed in crystal-mobile polymers, being referred to as α_c-relaxation.[38] Such a peak has already been reported before by Xia et al.[14] in a P(3HB-co-4HB) copolymer but could not yet be connected to possible ICD. A detailed discussion, specifically the confirmation of the observation of actual α_c-relaxation through master-curve

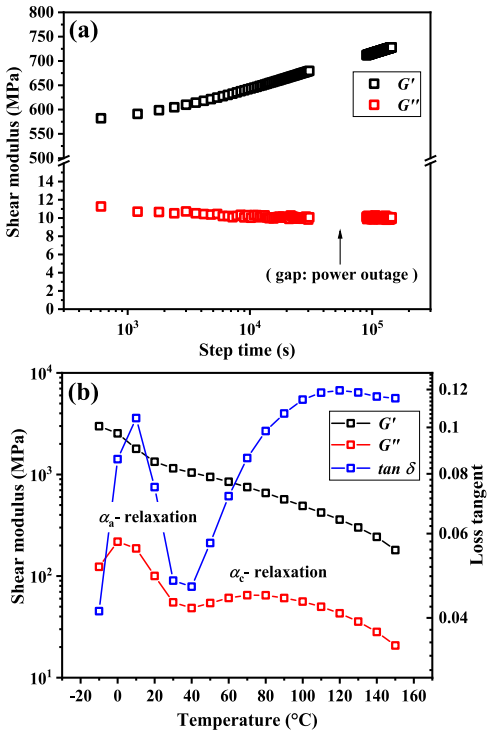

Figure 3. (a) G' and G'' measured by DMA during annealing at 60 °C, with a frequency of 10 rad/s and a strain of 0.1%. The specimen was isothermally crystallized at 120 °C for 1 h and then quickly cooled to room temperature and transferred to the DMA instrument. (b) G', G'' and tan δ measured by DMA in the temperature range from −10 to 150 °C, with a frequency of 0.1 rad/s and strain amplitude of 0.1%. The specimen was nonisothermally crystallized at an estimated cooling rate of 5 K/min.

construction and the relation to NMR observations of ICD, will be taken up below.

Semicrystalline Morphology. As P3HB embrittlement may be related to a change of crystallinity over time, SAXS was used to investigate the semicrystalline morphology of P3HB that was subjected to the same temperature profile as the samples studied mechanically. Specifically, we are interested in the crystalline and amorphous thicknesses, d_c and d_a, respectively, as well as their distributions, observed during isothermal crystallization at 120 °C for about 1 h and subsequent annealing at 60 °C for 4 days. This information is complemented by the calorimetric studies providing the melting point and an alternative measure of crystallinity by NMR, which will be discussed below.

Figure 4 shows the SAXS results of P3HB during isothermal crystallization at 120 °C. We observe that d_c and d_a are subject to thickening and thinning over time, respectively. The sample temperature was then reduced to 60 °C to observe the presence of possible crystal thickening via secondary crystallization at lower temperatures, mimicking possible slow changes at room temperature on an accelerated time scale, as also illustrated in Figure 4. The data reveal an ongoing thickening of P3HB crystal lamellae even after about 4 days. While the observed effects appear small (i.e., d_c increases from 5.1 to 5.9 nm and d_a decreases by about the same amount), the linear crystallinity $\phi_{SAXS} = d_c/(d_c + d_a)$ in fact increases from 0.62 to 0.72. Notably, the Porod parameter remains unchanged, confirming that the lamellar stack is largely conserved.

https://doi.org/10.1021/acs.macromol.4c00938
Macromolecules 2024, 57, 8507−8518

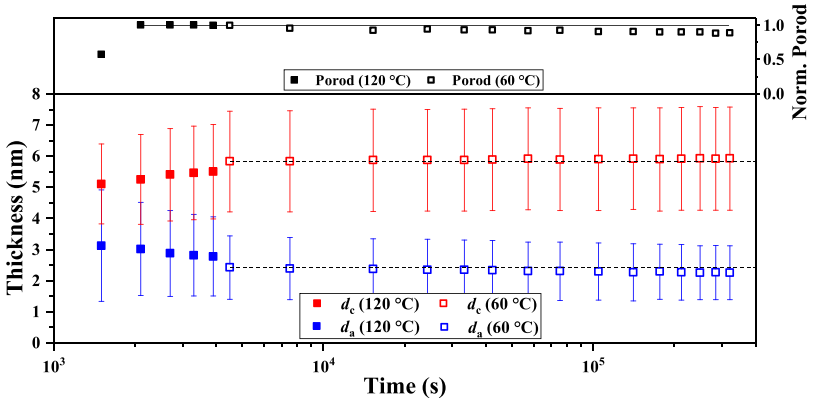

Figure 4. Thickness of crystalline (d_c) and amorphous (d_a) layers during the course of isothermal crystallization at 120 °C and during subsequent annealing at 60 °C for 3−4 days. The horizontal dashed lines guide the eye. Note that the "error bars" correspond to the width of the fitted thickness distributions, $\sigma_{c,a}$. The upper panel shows the evolution of the Porod parameter, confirming a constant interfacial area and thus a constant number of lamellae.

We note that the long period $L = d_a + d_c$ stays constant at around 8.2 ± 0.04 nm, which may be taken as evidence of actual lamellar thickening rather than insertion crystallization. In the latter case, all structural parameters $d_{a,c}$ and L would rather decrease.[40] Other important observations are the significant width of the d_c distribution as well as the narrower and still decreasing distribution width of d_a, which, together with the high crystallinity, are prototypical morphological features observed for polymers that feature slow ICD.[37,38]

These changes may well be held responsible for the observed embrittlement, although we lack an explicit model that connects these morphological changes with brittle failure. One possible connection could be through a higher confinement-induced T_g in the narrower amorphous gaps after aging/postcrystallization, explaining the positive effect of blending or using plasticizers.[9−13] The presence of tie chains and entanglements in the amorphous phase is also known to greatly affect the nonlinear mechanical properties of semicrystalline polymers. It is thus instructive to compare the coil dimensions and the entanglement spacing, estimated from $M_w \approx 4 \times 130$ kDa and the entanglement molecular weight M_e of about 4 kDa[48] to the SAXS-based dimensions. With $\langle R_g^2 \rangle_0 / M_w = 1.05 \times 10^{-3}$ nm^2 for the unperturbed dimensions of P3HB estimated from light-scattering studies,[49] we estimate the end-to-end distances R and R_e to be about 23 and 2 nm, respectively. Since R is thus significantly larger than twice the long period,[50] one can conclude on substantial contributions from both tie chains and conserved entanglements[51] in the amorphous phase.

Primary and Secondary Crystallization. Further confirmation of lamellar thickening as a relevant process during aging rather than an insertion mode is taken from FSC measurements, with which reliable melting temperatures (T_m) are determined for samples crystallized/aged at different times. The heating protocol is listed in Figure 5a. Figure 5b displays heating curves obtained after isothermal crystallization at 120 °C at different times. The increase in the area of the melting peaks plotted in the inset reflects the increase in crystallinity, while the peak temperature provides information about the crystal stability/thickness. It takes approximately 700 s for P3HB to finish its primary crystallization (bold black curve), after which the crystallinity increases with a different, much lower rate (see again the inset). Subsequently, secondary crystallization (red data) starts and is observed for up to

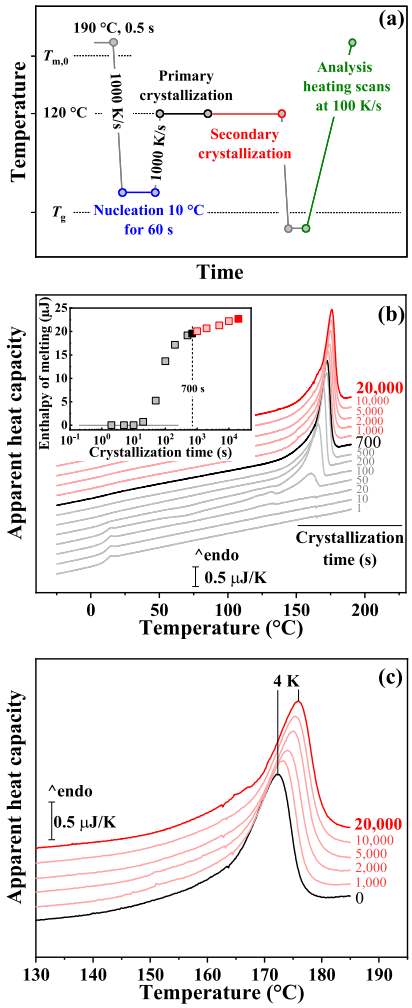

Figure 5. (a) Temperature protocol for the FSC. (b) Heating curves obtained after isothermal crystallization at 120 °C for different times. The primary and secondary crystallization processes are presented as gray/black and red curves. (c) Close-up of the changes after the completion of primary crystallization at 700 s (indicated as bold black curve). The inset in (b) shows the peak areas, reflecting the evolution of crystallinity.

https://doi.org/10.1021/acs.macromol.4c00938
Macromolecules 2024, 57, 8507−8518

20,000 s (5.5 h). As time progresses, the melting peak shifts to higher temperatures by 4 K; see Figure 5c.

The shifts in the melting temperature imply the internal perfectioning or thickening of lamellar crystals during secondary crystallization.[52−55] The absence of annealing peaks, furthermore, suggests the absence of distinct insertion crystallization, as was observed, e.g., for poly(butylene succinate), PBS, or PLA.[56,57] Another important feature of the FSC results is the presence of only one melting peak, which is not commonly observed for other polymers. For instance, FSC measurements on PBS and poly(butylene terephthalate) revealed multiple melting peaks, indicating substantial reorganization (melting and recrystallization) during heating.[52,58] However, for polymers that feature an α_c-process and ICD, such as poly(ethylene oxide), single melting peaks are typically observed.[59]

To emulate our aging experiments, we also studied the effect of aging at 60 °C after the completion of primary crystallization at 700 s, where within the same 5.5 h, only a smaller shift of 1.5 K is observed, as shown in Figure S3b. This is consistent with a significantly slowed-down thickening process, to be confirmed by our NMR studies. With all of this, we can be reasonably sure that ICD-mediated lamellar thickening is the mechanism of both secondary crystallization and the aging process characterized by SAXS. For this reason, we focus the following on samples that were not explicitly aged but simply isothermally crystallized, most of them for times well beyond primary crystallization, allowing for some thickening to occur.

On the side, we note that the DSC traces in Figure 5 confirm a T_g step somewhat below room temperature and a significant broadening and thus near-disappearance upon primary and secondary crystallization. Derivative analysis of the remaining weak feature indicates a shift of the main T_g step by 1−2 K during secondary crystallization. Further analyses regarding the possible appearance of a rigid-amorphous fraction are beyond our scope, but we can conclude that the DSC observations confirm at least a weak confinement effect, emphasizing the possible role of sluggish dynamics near T_g of the amorphous phase for the ultimate properties of P3HB at room temperature.

Temperature-dependent Crystallinity. The P3HB semicrystalline structure was further examined through measurements of the temperature dependence of the crystallinity up to the melting point. Figure 6 shows such data for samples that were isothermally crystallized for 1 h at different T_c values monitored by ^{1}H FID NMR, with additional data points from SAXS (only the 150 °C sample was crystallized for 5 h). For NMR, points upon cooling and subsequent heating were taken roughly every 10 min, while for SAXS, the data were taken only after isothermal crystallization and in one case after quenching to 60 °C, corresponding to the data in Figure 4. It should be noted that a reliable crystallinity can be determined with the NMR method only at or above 70 °C, as the measurement temperature needs to be a least 30 K above T_g of the amorphous phase, so as to impart sufficient mobility to significantly average dipole−dipole couplings and observe a sufficiently long and distinct T_2.

The results show that the P3HB crystallized at 140 °C exhibits a crystallinity of around 67% at that temperature, which then slowly rises to 83% after cooling to 70 °C. The increase is partially reversible, reaching 72% when the sample is heated back to 140 °C. Such a (partially) reversible lamellar

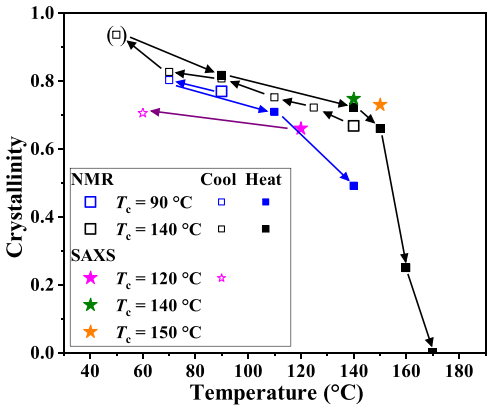

Figure 6. Crystallinity of the melt-crystallized P3HB was determined by NMR (squares) and SAXS (stars). The crystallization temperatures are indicated in the legend. The bracketed point indicates an unreliably high apparent crystallinity, see the text. While the noise-related fitting uncertainties are smaller than the symbol size, systematic errors related to the approximate/empirical nature of eq 4 may amount to about 5%.

thickening has also been observed for poly(ethylene),[60] the most prominent polymer exhibiting ICD.[27] The rather small changes in the crystallinity of P3HB prepared at high T_c over a wide temperature range suggest the existence of an overall well-defined and stabilized structure, which is again typical for crystal-mobile polymers. This stands in contrast to crystal-fixed polyesters such as poly(caprolactone), where reorganization phenomena impart a much stronger T-dependence.[37]

Finally, the high overall crystallinity and its marked increase with increasing T_c as evidenced from the SAXS results are again features that are typical for crystal-mobile polymers.[27,37] We also notice a satisfactory agreement between NMR and SAXS crystallinities for samples with comparable thermal histories, which differ only by a few percent. This confirms the reliability of both methods, which are after all based upon very different principles (mobility-based vs electron-density-based linear crystallinity from an assumed stack structure, respectively).

Intracrystalline Chain Diffusion. From the results so far, we have strong indications of the presence of an α_c-relaxation, c.f. Figure 3b, and the resulting ICD, constituting the origin of crystal thickening. The α_c-relaxation is commonly attributed to helical jumps of the chains within the crystals,[27] mediated by traveling defects.[61] Our previous work has clearly shown that the time scale of ICD, in relation to the time it takes a stem to be added to the growth front, decides whether crystal thickening already occurs during primary crystallization or only at much longer times in the secondary crystallization regime.[37,38] The relevant time scale is here the jump correlation time τ_c, which is the average residence time of a monomer in a given crystal raster position. With regard to a simple NMR-based detection, jumps faster than about 100 μs lead to motional averaging of proton−proton dipole−dipole couplings and can be observed by temperature-dependent changes in the crystalline component of low-resolution NMR FIDs.[40] Figure 7 actually shows only minimal changes arising from thermal expansion; τ_c must thus exceed 100 μs at any relevant temperature. Corresponding conclusions were already drawn recently by Xia et al. for the case of a P(3HB-co-4HB) sample.[14]

https://doi.org/10.1021/acs.macromol.4c00938
Macromolecules 2024, 57, 8507−8518

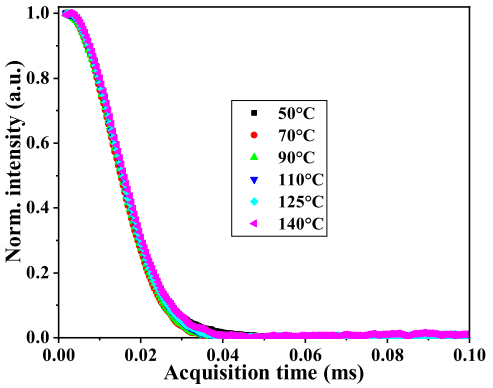

Figure 7. Normalized crystalline components of MSE-refocused FID signals after the subtraction of fitted amorphous components of P3HB, isothermally crystallized for 1 h at 140 °C.

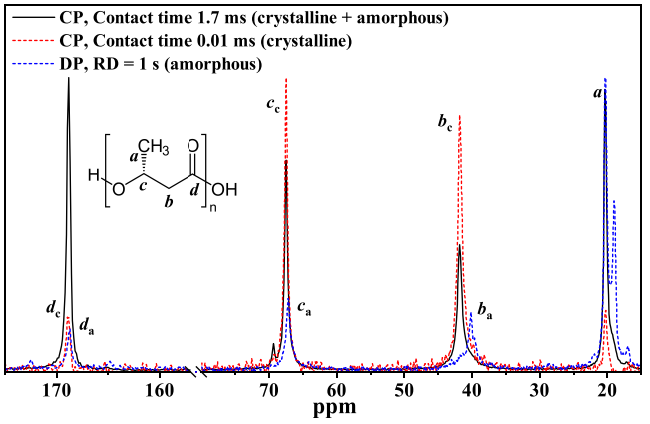

Figure 8. Comparison of selective ^{13}C MAS spectra of P3HB (T_c = 140 °C). The ^{13}C assignment is displayed in the inset; crystalline and amorphous resonances are assigned with subscripts c and a.

We thus turn to probing slow motions by observing ^{13}C CSA tensor re-orientations as well as the possibility of an exchange between ^{13}C isotropic chemical shifts between crystal and amorphous regions, provided they are distinguishable or by ^{13}C T_1 relaxation. Prior to these measurements, it is vital to determine which of the ^{13}C resonances is reliably attributed to the crystalline region. Figure 8 presents a combination of ^{13}C MAS spectra to assign the ^{13}C resonances and differentiate the ones originating from either the crystalline or amorphous region. As discussed in the Experimental Section, CP MAS with a 1.7 ms contact time enhances all ^{13}C resonances, while a 0.01 ms contact time (red dashed) and DP spectra with a 1 s recycle delay (blue short-dashed) are dominated by crystalline and amorphous resonances, respectively. The crystalline methyl peak was also detected by DP due to fast T_1 relaxation caused by methyl rotation. Thus, the crystalline peaks b_c, c_c, and d_c are utilized to probe possible slow mobility within the P3HB crystals.

As P3HB exhibits a 2_1 helical structure in its crystals,[62,63] resulting in a variation of CSA tensor orientations from monomer to monomer, the detection of slow chain mobility in the CSA-based CODEX technique should be possible,[29] as explained in the Experimental Section. Prior to determining the ICD time scale, an $N\tau_r$-dependent experiment was performed so as to choose the appropriate recoupling time ($N\tau_r$) for full sensitivity of monomer-jump detection. A long τ_{mix} of 5 s was used to ensure the occurrence jumps, hopefully reaching a detailed balance. Figure 9a demonstrates the expected intensity decay (actually proving already the presence of jumps), where for $N\tau_r$ longer than 0.2 ms, S/S_0 reaches a plateau value of about 0.4. A plateau of 0.5 is expected for two-site jumps in detailed balance; a lower value could be attributed to a higher number of distinguishable sites, which is hardly plausible. We attribute the lower value to $^{13}C-^{13}C$ spin diffusion, which mimics an exchange effect and is relevant for τ_{mix} exceeding 1 s.[29]

The shape of the $N\tau_r$ dephasing curves depends on the CSA principal values and the effective reorientation angle of the tensor in the two-site jump (see Figure 9b for a rendering). We refrained from modeling the curves, as CSA tensor information is not available for the given polymer. We notice a much faster dephasing for the carbonyl resonance d_c, which is expected due to its much wider CSA tensor. We also notice an undershoot of S/S_0 at $N\tau_r \approx 0.4$ ms for the other resonances, which is an actual feature of the given powder-averaged dephasing curves[29] (for the C=O resonance, it is likely located below 0.1 ms).

Figure 9c shows the τ_{mix}-dependent data with $N\tau_r$ = 0.3 ms, observing a monomer jump occurring approximately every 0.1 s within the crystalline lamellae of P3HB crystallized and measured at 120 °C. Stretched-exponential fits to the data (eq 6) provide the apparent jump correlation times τ_c^{KWW}; see the solid lines in Figure 9c. The relevant fitted parameters are indicated in the figure, while the stretching exponents β were in the range of 0.6 to 0.75. One can notice the onset of spin diffusion at times exceeding 1 s. The plateau of 0.5 for just the jumps is now clearly observed for the C=O peak d_c (dashed petrol line). The lower plateau of the other two peaks (dashed

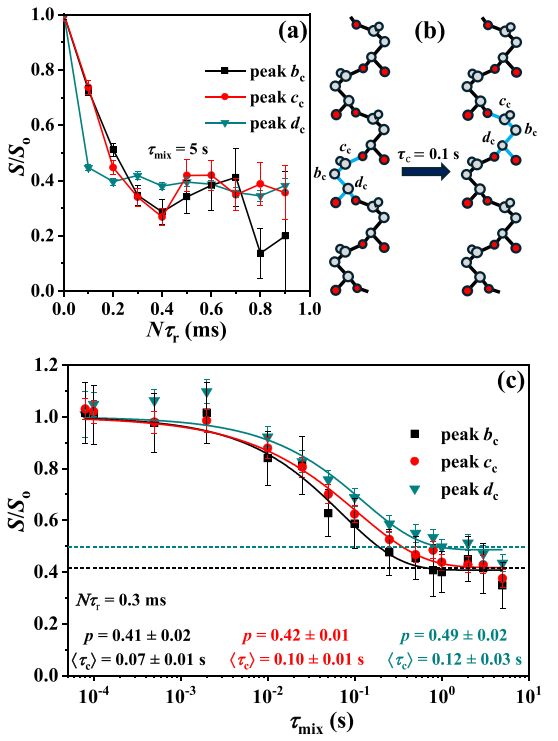

Figure 9. (a) $N\tau_r$-dependence of the normalized CODEX signal of different resonances with τ_{mix} = 5 s; (b) crystalline helix with selected marked carbons before and after one helical jump; (c) τ_{mix}-dependence to probe the time scale of monomer jumps. The sample was crystallized and measured at 120 °C.

https://doi.org/10.1021/acs.macromol.4c00938
Macromolecules 2024, 57, 8507−8518

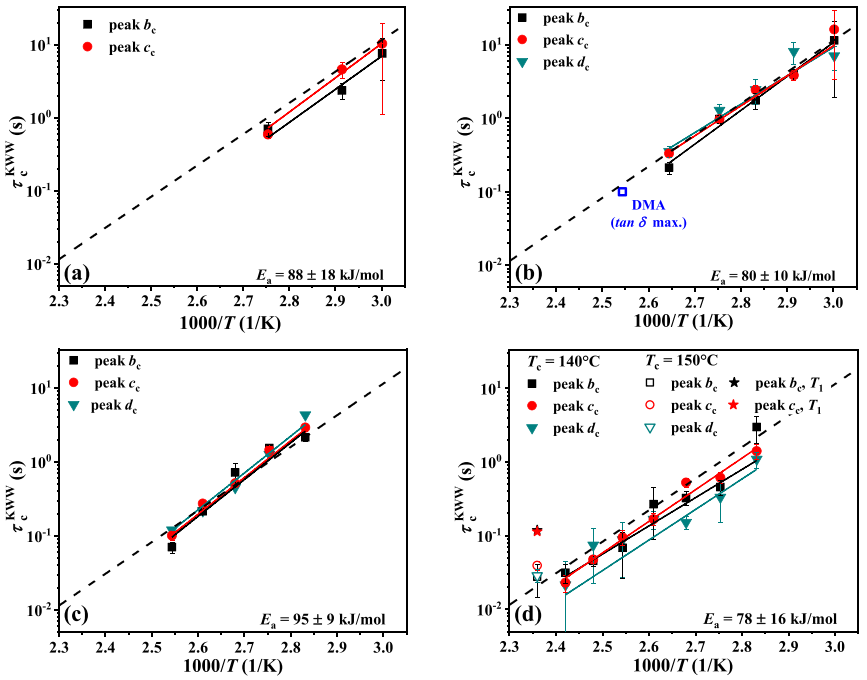

Figure 10. Arrhenius plots of τ_c^{KWW} in P3HB isothermally crystallized at (a) 90 °C, (b) 105 °C, (c) 120 °C, and (d) 140 °C. All plots have the same axes scaling with an identical dashed black line to aid a direct comparison. Part (b) also shows the inverse maximum position $1/\omega_{max}$ of tan $\delta(\omega)$, see Figure S4. In part (d) we also include jump times derived from the T_1-based measurements of large-scale chain transport, see Figure 11.

black line) is now explained by the location of the 0.3 ms recoupling time near the local minimum of the dephasing curve. Reassuringly, the τ_c^{KWW} of all peaks roughly match.

By measuring the helical-jump time at different temperatures, the apparent activation energies E_a of P3HB crystallized at different temperatures were obtained via Arrhenius plots, as illustrated in Figure 10. We refer to E_a as an "apparent" value, as we only cover a too-small temperature range and cannot decide whether a single molecular vs a cooperative process is studied. The defect-diffusion picture, with defect generation possibly taking place in the fold surface, actually points to a more complicated, multistep process.[61] The results show that E_a of P3HB is independent of the crystallization temperatures and within the range of 80−90 kJ/mol, while the absolute values of τ_c^{KWW} are similar for all samples, i.e., in the range of 0.8 to 2 s at 85 °C.

Before proceeding with comparisons and further interpretations, we should discuss the problem of choosing the appropriate characteristic correlation time,[64] considering the significant distribution reflected in the stretching exponents β. A common approach is the calculation of an arithmetic average of $\langle\tau_c\rangle = (\tau_c^{KWW}/\beta)\Gamma(1/\beta)$, given by the integral over the KWW function. A comparison of Arrhenius plots using τ_c^{KWW} vs $\langle\tau_c\rangle$ is shown in Figure S6. The latter data provide almost the same activation energy, but since the β values have comparably higher uncertainty due to the limited range of τ_{mix} and the onset of spin diffusion, the results scatter more significantly. For wide distributions, $\langle\tau_c\rangle$ is also biased strongly toward the slow end of the distribution, which may not represent a good physical choice. As pointed out by Zorn,[64] a logarithmic average $(\exp\{\langle\ln\tau_c^{KWW}\rangle\})$ is more appropriate, also because it reflects an arithmetic average of the relevant activation energy. In our earlier work on ICD in poly(ethylene),[41,65] the calculation and interpretation of $\langle\tau_c\rangle$ indeed led to less consistent conclusions than using log-scale averages, as pointed out in the two Corrections to these publications.[42,66] In the given range of β values, the logarithmic averages deviate by less than 30% from the fitted τ_c^{KWW},[64] which is why we stick to the latter as the appropriate characteristic jump correlation time τ_c.

To continue with the interpretation of the results, the CODEX-based activation energy can be compared to the one available from the DMA experiments on the compression-molded plate of nonisothermally crystallized P3HB, see Figure 3b. Focusing on the region of the α_c-relaxation, it is possible to construct a master curve via time−temperature superposition, as illustrated in Figure S4. This proves that an actual relaxation process is indeed observed, with the T-dependent shift factors providing an activation energy of 82 kJ/mol, in very favorable agreement with the NMR results. Moreover, even the relaxation time taken from the maximum position of tan $\delta(\omega)$ in the master curve (Figure S4), added in Figure 10b, perfectly matches the NMR data. While the good agreement may also be coincidental, it may show that the molecular back-and-forth jumps of the helix in the crystal have a direct coupling to the macroscopic mechanical response. We thus clarified the molecular details of the mechanical α_c-relaxation.

Given the range of τ_c values in Figure 10, it is surprising that Xia et al.[14] failed to observe such a slow process with the same CODEX technique. The sample used a fixed mixing time of 500 ms and checked temperatures up to 100 °C, at which our samples have τ_c values of a few hundred ms. We suspect that their measurements may have been subject to large T_2-related signal loss as a recoupling time of 2 ms was used, which is much larger than our best choice of 0.3 ms. We can also not exclude that their sample, prepared by film casting from solution, evaporation, and annealing at room temperature, may not be comparable to ours.

To finally establish the connection to the lamellar thickening via chain "sliding diffusion", we turn to probe the actual

https://doi.org/10.1021/acs.macromol.4c00938
Macromolecules 2024, 57, 8507−8518

exchange of monomers between the crystalline and amorphous regions. This is enabled by ^{13}C T_1 relaxation measurements,[44,45,65,66,68] harnessing the very long T_1 of the crystalline segments and the rather short T_1 in the amorphous phase. Diffusive exchange can thus be observed in terms of a nonexponential signal decay following initially a $\sqrt{\tau}$ dependence,[45,68] simply because chain diffusion into the fast-relaxing amorphous phase governs the signal loss.

Figure 11 displays a T_1 relaxation decay curve of P3HB crystallized for 24 h and measured (taking another day) at 150 °C after a comparably short CP contact time of 0.1 ms, plotted on a $\sqrt{\tau}$ axis scale. The shorter CP serves to reduce signals from the amorphous component, to simplify the deconvolution of the spectra. The data exhibits a linear decay with $\sqrt{\tau}$ in the initial part of the graph, emphasizing diffusive behavior. This stands in contrast to the (multi)exponential decay of crystal-fixed polymers, here exemplified by direct comparison with earlier results on PBS,[67] which clearly show an initial curvature. The trend toward a plateau value for P3HB at longer ^{13}C T_1 exchange times can be attributed to restrictions to chain diffusion by entanglements in the amorphous region.[45]

Assuming the 1D free-diffusion behavior, the initial decay can be written as follows:[65,68−70]

$$\frac{I(\tau)}{I(\tau=0)} \approx 1 - \frac{\sqrt{2D}}{d_c}\sqrt{\tau} \tag{7}$$

where $I(\tau)/I(\tau = 0)$ is the normalized decay intensity and D is the diffusion coefficient of the chain along the stem direction. For an even clearer visualization, eq 7 can be rewritten as

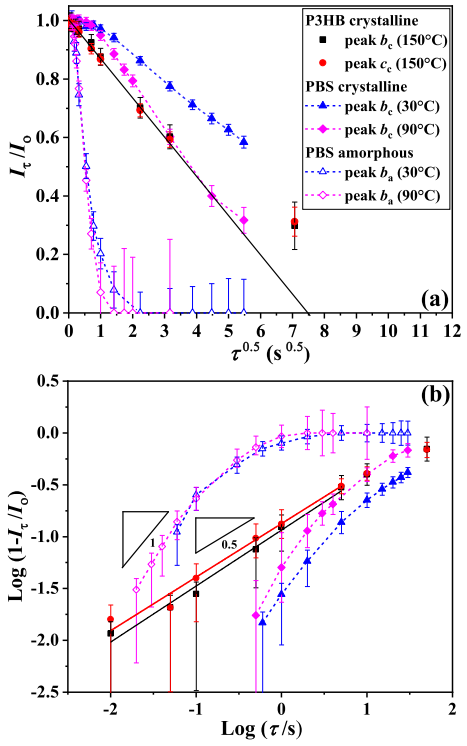

Figure 11. T_1 relaxation decay measurements of P3HB crystallized and measured at 150 °C, plotted in two different ways following (a) eq 7 and (b) eq 8, respectively. The solid lines are fits to the respective equations, considering the initial data points. PBS data from previous work[67] is added here as a comparison for the crystal-fixed case.

$$\log\left(1 - \frac{I(\tau)}{I(\tau=0)}\right) \approx \frac{1}{2}\log\tau + \log\frac{\sqrt{2D}}{d_c} \tag{8}$$

which serves as a basis of a log−log plot, Figure 11b, that immediately reveals the diffusive 1/2 power-law exponent in the initial rise. In contrast to the crystalline resonances of P3HB, the data for its amorphous phase and the data for the crystalline resonances of PBS show an exponent of 1, as expected for exponential functions having a Taylor expansion with a linear leading term.

The solid lines in Figure 11a,b are fits to the initial linearized regions using eqs 7 and 8, respectively, using d_c = 8.34 nm as obtained by SAXS. Then, using the Einstein−Smoluchowsky equation for 1D diffusion ($\langle z^2\rangle = 2D\tau_{step}$), equating $\langle z^2\rangle$ with the squared projection length of a single monomer along the stem direction (0.385 nm) taken from the crystal structure,[62,63] we can convert the fitted D value into a diffusion-based estimate of the monomer jump time, τ_{step}, to be compared to $<\tau_c>$ from CODEX. Both fits give a monomer jump time of around 0.12 s, as compared to 0.03 s obtained by CODEX. Both data points are added in Figure 10d.

The longer jump time obtained from ^{13}C T_1 relaxation can be well explained in three ways, first by an influence of entanglement constraints in the amorphous phase once the displacement becomes larger than a few monomer jumps,[45] second by the neglect of a possible chain tilt in the lamellae (making the stem length larger than d_c from SAXS), and third by the correlation time distribution. Stretching exponents β fitted to the CODEX data, which clustered in the range between 0.6 and 0.75, indicate significant distributions, similar to those found for poly(ethylene)[65,66] and poly(ethylene oxide).[61] It is reasonable to assume that the correlation time back-calculated from the large-scale 1D diffusion, requiring many helical jumps, is biased toward the longer jump correlation times in the distribution. The comparison shown in Figure S6 supports this argument.

CONCLUSIONS

In conclusion, we have found that the well-documented embrittlement of P3HB, i.e., a significant reduction of the strain at break and a slow increase of the shear modulus upon aging at room temperature, can also be achieved by higher-temperature annealing at 60 °C. Under these conditions, SAXS results indicate that the crystalline thickness slowly rises, the amorphous thickness slowly decreases and its distribution narrows, while FSC results reveal a gradual increase of the melting point during secondary crystallization at 120 °C. Both methods show that during further aging at 60 °C, the sample keeps changing in the same way, but simply on a much longer time scale.

All these observations are in line with P3HB being a crystal-mobile polymer, where intracrystalline chain diffusion (ICD) enables lamellar thickening during primary as well as secondary crystallization, as established by our recent publications.[37,38] While we lack a model to explain the mechanistic connection between embrittlement and the observed morphology changes, it can be hypothesized that the glass transition temperature in the increasingly small amorphous domains, being generally close to room temperature, increases due to confinement effects, leading to brittle rather than elastic contributions to the overall mechanical response. Alternatively, considering the large expected contribution of tie chains and entanglements in

https://doi.org/10.1021/acs.macromol.4c00938
Macromolecules 2024, 57, 8507−8518

the amorphous phase to the deformation behavior of the given P3HB, one might also envisage some degree of loss of entanglements and tie chains due to the ICD and the corresponding possibility of large-scale reptation motion. Another possibility would be that during aging densification of the material may lead to the formation of small microcracks, making the material more sensitive for fracture.

The last and central part of this work has been concerned with molecular-level proof of the presence of ICD by different NMR techniques. The CODEX experiment reveals the presence of comparably slow helical jumps with an average correlation $\langle\tau_c\rangle$ of about 0.1 s at 120 °C. Apparent jump activation energies E_a ranged between 80 and 90 kJ/mol, with both the absolute time scale and E_a being independent of the crystallization temperature T_c of the sample. With this, the $\langle\tau_c\rangle$ values in the range of typical T_c are about 2 orders of magnitude larger than in the previously studied case of poly(oxymethylene), where consequently, the lamellae thicken more significantly during primary crystallization.[38] While many if not most polyesters are crystal-fixed,[27,37,67] P3HB seems to be the second prominent exception, alongside the α phase of stereoregular PLA,[71] which features similar jump correlation times at typical T_c.

Finally, the connection between the helical jumps and the large-scale diffusive exchange between the crystalline and amorphous regions is confirmed by ^{13}C T_1 relaxation measurements. Here, we also introduced a more robust distinction between magnetization decay by chain diffusion vs actual T_1 relaxation by using a log−log plot of the normalized signal decay during a z filter: $\log(1 - I(\tau)/I(\tau = 0))$ vs $\log(\tau)$. In this plot, the slope immediately reveals a diffusive power-law exponent of 0.5, while the 1D intracrystalline chain diffusion coefficient is encoded in the intercept, requiring knowledge of the SAXS-based lamellar thickness.

In summary, and in contrast to the recent claim of Xia et al.,[14] we have identified P3HB as a crystal-mobile polymer. While the possible relation between the observed ICD, the lamellar thickening, and the embrittlement remains an open question, we anticipate the development of more focused strategies to improve the mechanical properties of this fascinating material, e.g., by copolymerization with monomers that do not fit the crystals and thus limit lamellar thickening, in analogy to similar strategies that are well-established for, e.g., poly(ethylene).

■ ASSOCIATED CONTENT

Data Availability Statement

The data sets generated and analyzed for this study as they appear in the figures of this article and the Supporting Information can be found in the Zenodo repository: 10.5281/zenodo.11115448.

Supporting Information

The Supporting Information is available free of charge at https://pubs.acs.org/doi/10.1021/acs.macromol.4c00938.

Details on DSC experiments and sample aging (Figure S1), SAXS measurements and analyses details (Figure S2), FSC experiments and annealing effect (Figure S3), rheological characterization of the α_c relaxation of nonisothermally crystallized P3HB (Figure S4), rheological characterization of the α_c relaxation of HDPE (Figure S5), comparison of fitted and first-moment averaged correlation times (Figure S6) (PDF)

■ AUTHOR INFORMATION

Corresponding Authors

Thomas Thurn-Albrecht − *Institut für Physik, Martin-Luther-Universität Halle-Wittenberg, 06099 Halle (Saale), Germany*; orcid.org/0000-0002-7618-0218; Phone: +49-345-55-28560; Email: thomas.thurn-albrecht@physik.uni-halle.de; Fax: +49-345-55-27161

Kay Saalwächter − *Institut für Physik, Martin-Luther-Universität Halle-Wittenberg, 06099 Halle (Saale), Germany*; orcid.org/0000-0002-6246-4770; Email: kay.saalwaechter@physik.uni-halle.de

Authors

Afiq Anuar − *Institut für Physik, Martin-Luther-Universität Halle-Wittenberg, 06099 Halle (Saale), Germany*

Qiang Yu − *Institut für Physik, Martin-Luther-Universität Halle-Wittenberg, 06099 Halle (Saale), Germany*

Katalee Jariyavidyanont − *Interdisziplinäres Zentrum für Transferorientierte Forschung in den Naturwissenschaften (IWE TFN), Martin-Luther-Universität Halle-Wittenberg, 06099 Halle (Saale), Germany*; orcid.org/0000-0001-8240-126X

Albrecht Petzold − *Institut für Physik, Martin-Luther-Universität Halle-Wittenberg, 06099 Halle (Saale), Germany*; orcid.org/0000-0002-2920-7019

René Androsch − *Interdisziplinäres Zentrum für Transferorientierte Forschung in den Naturwissenschaften (IWE TFN), Martin-Luther-Universität Halle-Wittenberg, 06099 Halle (Saale), Germany*; orcid.org/0000-0002-7924-0159

Complete contact information is available at: https://pubs.acs.org/10.1021/acs.macromol.4c00938

Notes

The authors declare no competing financial interest.

■ ACKNOWLEDGMENTS

Financial support by the Deutsche Forschungsgemeinschaft (DFG) in the framework of the SFB-TRR 102 (project-ID 189853844, project A1) is gratefully acknowledged. R.A. and K.J. acknowledge additional financial support by the DFG through grants AN 212/26 and AN 212/29. The authors thank Urs Hänggi (Biomer, Schwalbach, Germany) for providing the samples and valuable comments on the manuscript.

■ REFERENCES

(1) McAdam, B.; Brennan Fournet, M.; McDonald, P.; Mojicevic, M. Production of polyhydroxybutyrate (PHB) and factors impacting its chemical and mechanical characteristics. *Polymers* **2020**, *12*, 2908.

(2) Suzuki, M.; Tachibana, Y.; Kasuya, K.-i. Biodegradability of poly (3-hydroxyalkanoate) and poly (ε-caprolactone) via biological carbon cycles in marine environments. *Polym. J.* **2021**, *53*, 47−66.

(3) De Koning, G.; Lemstra, P. Crystallization phenomena in bacterial poly [(R)-3-hydroxybutyrate]: 2. Embrittlement and rejuvenation. *Polymer* **1993**, *34*, 4089−4094.

(4) Lizarraga-Valderrama, L. R.; Nigmatullin, R.; Taylor, C.; Haycock, J. W.; Claeyssens, F.; Knowles, J. C.; Roy, I. Nerve tissue engineering using blends of poly (3-hydroxyalkanoates) for peripheral nerve regeneration. *Engineering in Life Sciences* **2015**, *15*, 612−621.

(5) Gregory, D. A.; Taylor, C. S.; Fricker, A. T.; Asare, E.; Tetali, S. S.; Haycock, J. W.; Roy, I. Polyhydroxyalkanoates and their advances for biomedical applications. *Trends in Molecular Medicine* **2022**, *28*, 331−342.

(6) Srubar, W., III; Wright, Z.; Tsui, A.; Michel, A.; Billington, S.; Frank, C. Characterizing the effects of ambient aging on the mechanical and physical properties of two commercially available bacterial thermoplastics. *Polym. Degrad. Stab.* **2012**, *97*, 1922−1929.
(7) Zhang, L.; Deng, X.; Huang, Z. Miscibility, thermal behaviour and morphological structure of poly (3-hydroxybutyrate) and ethyl cellulose binary blends. *Polymer* **1997**, *38*, 5379−5387.
(8) Hobbs, J.; Sykes, K.; McMaster, T.; Barham, P. Monitoring degradation of poly (hydroxybutyrate) by fracture toughness measurements. *J. Environ. Polym. Degrad.* **1996**, *4*, 235−241.
(9) El-Hadi, A.; Schnabel, R.; Straube, E.; Müller, G.; Henning, S. Correlation between degree of crystallinity, morphology, glass temperature, mechanical properties and biodegradation of poly (3-hydroxyalkanoate) PHAs and their blends. *Polym. Test.* **2002**, *21*, 665−674.
(10) An, Y.; Dong, L.; Li, G.; Mo, Z.; Feng, Z. Miscibility, crystallization kinetics, and morphology of poly (β-hydroxybutyrate) and poly (methyl acrylate) blends. *J. Polym. Sci., Part B: Polym. Phys.* **2000**, *38*, 1860−1867.
(11) Verhoogt, H.; Ramsay, B.; Favis, B. Polymer blends containing poly (3-hydroxyalkanoate) s. *Polymer* **1994**, *35*, 5155−5169.
(12) An, Y.; Li, L.; Dong, L.; Mo, Z.; Feng, Z. Nonisothermal crystallization and melting behavior of poly (β-hydroxybutyrate)−Poly (vinyl-acetate) blends. *J. Polym. Sci., Part B: Polym. Phys.* **1999**, *37*, 443−450.
(13) Choi, J. S.; Park, W. H. Effect of biodegradable plasticizers on thermal and mechanical properties of poly (3-hydroxybutyrate). *Polym. Test.* **2004**, *23*, 455−460.
(14) Xia, Z.; Zhao, H.; Wang, Y.; Ma, Y.; Wang, X.; Meng, L.; Wang, D.; Sheng, J.; Chen, W. Chain dynamics and crystalline network structure of poly [R-3-hydroxybutyrate-co-4-hydroxybutyrate] as revealed by solid-state NMR. *Soft Matter* **2021**, *17*, 4195−4203.
(15) Zhou, Z.; LaPointe, A. M.; Shaffer, T. D.; Coates, G. W. Nature-inspired methylated polyhydroxybutyrates from C1 and C4 feedstocks. *Nat. Chem.* **2023**, *15*, 856−861.
(16) Zhou, L.; Zhang, Z.; Shi, C.; Scoti, M.; Barange, D. K.; Gowda, R. R.; Chen, E. Y.-X. Chemically circular, mechanically tough, and melt-processable polyhydroxyalkanoates. *Science* **2023**, *380*, 64−69.
(17) Ajellal, N.; Durieux, G.; Delevoye, L.; Tricot, G.; Dujardin, C.; Thomas, C. M.; Gauvin, R. M. Polymerization of racemic β-butyrolactone using supported catalysts: a simple access to isotactic polymers. *Chem. Commun.* **2010**, *46*, 1032−1034.
(18) Dong, X.; Robinson, J. R. The role of neutral donor ligands in the isoselective ring-opening polymerization of rac-β-butyrolactone. *Chemical Science* **2020**, *11*, 8184−8195.
(19) Tang, X.; Chen, E. Y.-X. Chemical synthesis of perfectly isotactic and high melting bacterial poly (3-hydroxybutyrate) from bio-sourced racemic cyclic diolide. *Nat. Commun.* **2018**, *9*, 2345.
(20) Yu, L.-P.; Yan, X.; Zhang, X.; Chen, X.-B.; Wu, Q.; Jiang, X.-R.; Chen, G.-Q. Biosynthesis of functional polyhydroxyalkanoates by engineered Halomonas bluephagenesis. *Metabolic engineering* **2020**, *59*, 119−130.
(21) Füchtenbusch, B.; Fabritius, D.; Steinbüchel, A. Incorporation of 2-methyl-3-hydroxybutyric acid into polyhydroxyalkanoic acids by axenic cultures in defined media. *FEMS microbiology letters* **1996**, *138*, 153−160.
(22) Watanabe, Y.; Ishizuka, K.; Furutate, S.; Abe, H.; Tsuge, T. Biosynthesis and characterization of novel poly (3-hydroxybutyrate-co-3-hydroxy-2-methylbutyrate): thermal behavior associated with α-carbon methylation. *RSC Adv.* **2015**, *5*, 58679−58685.
(23) Furutate, S.; Nakazaki, H.; Maejima, K.; Hiroe, A.; Abe, H.; Tsuge, T. Biosynthesis and characterization of novel polyhydroxyalkanoate copolymers consisting of 3-hydroxy-2-methylbutyrate and 3-hydroxyhexanoate. *J. Polym. Res.* **2017**, *24*, 221.
(24) Dong, H.; Liffland, S.; Hillmyer, M. A.; Chang, M. C. Engineering in vivo production of α-branched polyesters. *J. Am. Chem. Soc.* **2019**, *141*, 16877−16883.
(25) Furutate, S.; Abe, H.; Tsuge, T. Thermal properties of poly (3-hydroxy-2-methylbutyrate-co-3-hydroxybutyrate) copolymers with narrow comonomer-unit compositional distributions. *Polym. J.* **2021**, *53*, 1451−1457.
(26) Razavi, M.; Zhang, W.; Khonakdar, H. A.; Janke, A.; Li, L.; Wang, S.-Q. Inducing nano-confined crystallization in PLLA and PET by elastic melt stretching. *Soft Matter* **2021**, *17*, 1457−1462.
(27) Hu, W.-G.; Schmidt-Rohr, K. Polymer ultradrawability: the crucial role of α-relaxation chain mobility in the crystallites. *Acta polymerica* **1999**, *50*, 271−285.
(28) Strobl, G. *The Physics of Polymers*, 3rd revised ed.; Springer: Berlin, 2007.
(29) de Azevêdo, E. R.; Hu, W.; Bonagamba, T. J.; Schmidt-Rohr, K. Center band − only detection of exchange: efficient analysis of dynamics in solids by NMR. *J. Am. Chem. Soc.* **1999**, *121*, 8411−8412.
(30) Briassoulis, D.; Athanasoulia, I.-G.; Tserotas, P. PHB/PLA plasticized by olive oil and carvacrol solvent-cast films with optimized ductility and physical ageing stability. *Polym. Degrad. Stab.* **2022**, *200*, No. 109958.
(31) Hufenus, R.; Reifler, F. A.; Fernández-Ronco, M. P.; Heuberger, M. Molecular orientation in melt-spun poly (3-hydroxybutyrate) fibers: Effect of additives, drawing and stress-annealing. *Eur. Polym. J.* **2015**, *71*, 12−26.
(32) Omura, T.; Goto, T.; Maehara, A.; Kimura, S.; Abe, H.; Iwata, T. Thermal degradation behavior of poly [(R)-3-hydroxybutyrate-co-4-hydroxybutyrate]. *Polym. Degrad. Stab.* **2021**, *183*, No. 109460.
(33) Barham, P.; Keller, A.; Otun, E.; Holmes, P. Crystallization and morphology of a bacterial thermoplastic: poly-3-hydroxybutyrate. *J. Mater. Sci.* **1984**, *19*, 2781−2794.
(34) Schick, C.; Wurm, A.; Mohamed, A. Vitrification and devitrification of the rigid amorphous fraction of semicrystalline polymers revealed from frequency-dependent heat capacity. *Colloid Polym. Sci.* **2001**, *279*, 800−806.
(35) Ruland, W. The evaluation of the small-angle scattering of lamellar two-phase systems by means of interface distribution functions. *Colloid and polymer science* **1977**, *255*, 417−427.
(36) Seidlitz, A.; Thurn-Albrecht, T. Small-Angle X-ray Scattering for Morphological Analysis of Semicrystalline Polymers. *Polymer Morphology: Principles, Characterization, and Processing* **2016**, 151−164.
(37) Schulz, M.; Seidlitz, A.; Kurz, R.; Bärenwald, R.; Petzold, A.; Saalwächter, K.; Thurn-Albrecht, T. The underestimated effect of intracrystalline chain dynamics on the morphology and stability of semicrystalline polymers. *Macromolecules* **2018**, *51*, 8377−8385.
(38) Schulz, M.; Schäfer, M.; Saalwächter, K.; Thurn-Albrecht, T. Competition between crystal growth and intracrystalline chain diffusion determines the lamellar thickness in semicrystalline polymers. *Nat. Commun.* **2022**, *13*, 119.
(39) Rhim, W.-K.; Pines, A.; Waugh, J. S. Time-reversal experiments in dipolar-coupled spin systems. *Phys. Rev. B* **1971**, *3*, 684.
(40) Schäler, K.; Roos, M.; Micke, P.; Golitsyn, Y.; Seidlitz, A.; Thurn-Albrecht, T.; Schneider, H.; Hempel, G.; Saalwächter, K. Basic principles of static proton low-resolution spin diffusion NMR in nanophase-separated materials with mobility contrast. *Solid state nuclear magnetic resonance* **2015**, *72*, 50−63.
(41) Bärenwald, R.; Champouret, Y.; Saalwächter, K.; Schäler, K. Determination of Chain Flip Rates in Poly(ethylene) Crystallites by Solid-State Low-Field ^{1}H NMR for Two Different Sample Morphologies. *J. Phys. Chem. B* **2012**, *116*, 13089−13097.
(42) Bärenwald, R.; Champouret, Y.; Saalwächter, K.; Schäler, K. Correction to "Determination of Chain Flip Rates in Poly(ethylene) Crystallites by Solid-State Low-Field ^{1}H NMR for Two Different Sample Morphologies. *J. Phys. Chem. B* **2014**, *118*, 12575−12576.
(43) Fung, B.; Khitrin, A.; Ermolaev, K. An improved broadband decoupling sequence for liquid crystals and solids. *Journal of magnetic resonance* **2000**, *142*, 97−101.
(44) Torchia, D. A. The measurement of proton-enhanced carbon-13 T1 values by a method which suppresses artifacts. *J. Magn. Reson.* **1969**, *1978* (30), 613−616.

https://doi.org/10.1021/acs.macromol.4c00938
Macromolecules 2024, 57, 8507−8518

(45) Schmidt-Rohr, K.; Spiess, H. Chain diffusion between crystalline and amorphous regions in polyethylene detected by 2D exchange carbon-13 NMR. *Macromolecules* **1991**, *24*, 5288−5293.
(46) Czerniecka, A.; Magoń, A.; Schliesser, J.; Woodfield, B.; Pyda, M. Heat capacity of poly (3-hydroxybutyrate). *J. Chem. Thermodyn.* **2014**, *73*, 76−84.
(47) Wei, Z.; Liu, L.; Qi, M. Synthesis and characterization of homo- and co-polymers of (R, S)-β-butyrolactone and γ-butyrolactone or β-valerolactone initiated with cyclic tin alkoxide. *React. Funct. Polym.* **2006**, *66*, 1411−1419.
(48) Dorgan, J. R.; Janzen, J.; Clayton, M. P.; Hait, S. B.; Knauss, D. M. Melt rheology of variable L-content poly(lactic acid). *J. Rheol.* **2005**, *49*, 607−619.
(49) Hirosye, T.; Einaga, Y.; Fujita, H. Excluded-Volume Effects in Dilute Polymer Solutions. VIII. Poly(D,L-β-methyl β-propiolactone) in Several Solvents and Reanalysis of Data on Poly(D-β-hydroxybutyrate). *Polym. J.* **1979**, *11*, 819−826.
(50) Huang, Y.-L.; Brown, N. The effect of molecular weight on slow crack growth in linear polyethylene homopolymers. *J. Mater. Sci.* **1988**, *23*, 3648−3655.
(51) Kurz, R.; Schulz, M.; Scheliga, F.; Men, Y.; Seidlitz, A.; Thurn-Albrecht, T.; Saalwächter, K. Interplay between Crystallization and Entanglements in the Amorphous Phase of the Crystal-fixed Polymer Poly(ϵ-caprolactone). *Macromolecules* **2018**, *51*, 5831−5841.
(52) Toda, A.; Furushima, Y.; Androsch, R.; Schick, C. On the crystal stabilization during two-step isothermal crystallization of poly (butylene terephthalate) examined by fast scanning calorimetry. *Polymer* **2021**, *230*, No. 124057.
(53) Toda, A.; Taguchi, K.; Kono, G.; Nozaki, K. Crystallization and melting behaviors of poly (vinylidene fluoride) examined by fast-scan calorimetry: Hoffman-Weeks, Gibbs-Thomson and thermal Gibbs-Thomson plots. *Polymer* **2019**, *169*, 11−20.
(54) Toda, A.; Taguchi, K.; Nozaki, K. Gibbs−Thomson, thermal Gibbs−Thomson, and Hoffman−Weeks plots of polyethylene crystals examined by fast-scan calorimetry and small-angle X-ray scattering. *Cryst. Growth Des.* **2019**, *19*, 2493−2502.
(55) Toda, A.; Taguchi, K.; Nozaki, K.; Guan, X.; Hu, W.; Furushima, Y.; Schick, C. Crystallization and melting of poly (butylene terephthalate) and poly (ethylene terephthalate) investigated by fast-scan chip calorimetry and small angle X-ray scattering. *Polymer* **2020**, *192*, No. 122303.
(56) Schick, C.; Androsch, R. The origin of annealing peaks in semicrystalline polymers: Enthalpy recovery or melting? *Macromolecules* **2020**, *53*, 8751−8756.
(57) Androsch, R.; Toda, A.; Furushima, Y.; Schick, C. Insertion-Crystallization-Induced Low-Temperature Annealing Peaks in Melt-Crystallized Poly(L-Lactic Acid). *Macromol. Chem. Phys.* **2021**, *222*, 2100177.
(58) Androsch, R.; Jariyavidyanont, K.; Janke, A.; Schick, C. Poly (butylene succinate): Low-temperature nucleation and crystallization, complex morphology and absence of lamellar thickening. *Polymer* **2023**, *285*, No. 126311.
(59) Schulz, M.; Seidlitz, A.; Petzold, A.; Thurn-Albrecht, T. The effect of intracrystalline chain dynamics on melting and reorganization during heating in semicrystalline polymers. *Polymer* **2020**, *196*, No. 122441.
(60) Albrecht, T.; Strobl, G. Temperature-Dependent Crystalline-Amorphous Structures in Linear Polyethylene: Surface Melting and the Thickness of the Amorphous Layers. *Macromolecules* **1995**, *28*, 5827−5833.
(61) Kurz, R.; Achilles, A.; Chen, W.; Schäfer, M.; Seidlitz, A.; Golitsyn, Y.; Paul, W.; Hempel, G.; Kressler, J.; Miyoshi, T.; Thurn-Albrecht, T.; Saalwächter, K. Intracrystalline Jump Motion in Poly(ethylene oxide) Lamellae of Variable Thickness: A Comparison of NMR Methods. *Macromolecules* **2017**, *50*, 3890−3902.
(62) Yokouchi, M.; Chatani, Y.; Tadokoro, H.; Teranishi, K.; Tani, H. Structural studies of polyesters: 5. Molecular and crystal structures of optically active and racemic poly(β-hydroxybutyrate). *Polymer* **1973**, *14*, 262−267.
(63) Pazur, R. J.; Raymond, S.; Hocking, P. J.; Marchessault, R. H. Molecular modelling of helical and extended-chain polyhydroxybutyrates and polytetramethylene succinate. *Polymer* **1998**, *39*, 3065−3072.
(64) Zorn, R. Logarithmic moments of relaxation time distributions. *J. Chem. Phys.* **2002**, *116*, 3204−3209.
(65) Bärenwald, R.; Goerlitz, S.; Godehardt, R.; Osichow, A.; Tong, Q.; Krumova, M.; Mecking, S.; Saalwächter, K. Local flips and chain motion in polyethylene crystallites: a comparison of melt-crystallized samples, reactor powders, and nanocrystals. *Macromolecules* **2014**, *47*, 5163−5173.
(66) Bärenwald, R.; Goerlitz, S.; Godehardt, R.; Osichow, A.; Tong, Q.; Krumova, M.; Mecking, S.; Saalwächter, K. Correction to "Local Flips and Chain Motion in Polyethylene Crystallites: A Comparison of Melt-Crystallized Samples, Reactor Powders, and Nanocrystals. *Macromolecules* **2014**, *47*, 7677−7678.
(67) Yu, Q.; Anuar, A.; Petzold, A.; Balko, J.; Saalwächter, K.; Thurn-Albrecht, T. The semicrystalline morphology of polybutylene succinate supports a general scheme based on intracrystalline dynamics. *Macromol. Chem. Phys.* **2023**, *224*, No. 2200459.
(68) Yao, Y.; Graf, R.; Spiess, H. W.; Lippits, D.; Rastogi, S. Morphological differences in semicrystalline polymers: Implications for local dynamics and chain diffusion. *Phys. Rev. E* **2007**, *76*, No. 060801.
(69) Axelson, D.; Mandelkern, L.; Popli, R.; Mathieu, P. d. Carbon-13 NMR of polyethylenes: Correlation of the crystalline component T1 with structure. *J. Polym. Sci., Polym. Phys. Ed.* **1983**, *21*, 2319−2335.
(70) Yao, Y.; Graf, R.; Spiess, H.; Rastogi, S. Influence of crystal thickness and topological constraints on chain diffusion in linear polyethylene. *Macromol. Rapid Commun.* **2009**, *30*, 1123−1127.
(71) Chen, W.; Reichert, D.; Miyoshi, T. Helical Jump Motions of Poly(l-Lactic Acid) Chains in the α Phase As Revealed by Solid-State NMR. *J. Phys. Chem. B* **2015**, *119*, 4552−4563.

https://doi.org/10.1021/acs.macromol.4c00938
Macromolecules 2024, 57, 8507−8518